From Sphere Packing to the Theory of Optimal Lattice Sampling

Alireza Entezari, Ramsay Dyer, and Torsten Möller

Simon Fraser University, Burnaby, BC, Canada
{aentezar,rhdyer,torsten}@cs.sfu.ca

Summary. In this paper we introduce reconstruction kernels for the 3D optimal sampling lattice and demonstrate a practical realisation of a few. First, we review fundamentals of multidimensional sampling theory. We derive the optimal regular sampling lattice in 3D, namely the Body Centered Cubic (BCC) lattice, based on a spectral sphere packing argument. With the introduction of this sampling lattice, we review some of its geometric properties and its dual lattice. We introduce the ideal reconstruction kernel in the space of bandlimited functions on this lattice. Furthermore, we introduce a family of box splines for reconstruction on this sampling lattice. We conclude the paper with some images and results of sampling on the BCC lattice and contrast it with equivalent samplings on the traditionally used Cartesian lattice. Our experimental results confirm the theory that BCC sampling yields a more accurate discrete representation of a signal comparing to the commonly used Cartesian sampling.

1 Introduction

With the advent of the theory of digital signal processing various fields in science and engineering have been dealing with discrete representations of continuous phenomena. As scientific computing algorithms mature and find applications in a variety of scientific, medical and engineering fields, the question of the accuracy of the discrete representations gains an enormous importance. The theory of optimal sampling deals with this issue: given a fixed number of samples, how can one capture the most information from the underlying continuous phenomena. Such a sampling pattern would constitute the most accurate discrete representation.

While virtually all image and volume processing algorithms are based on the Cartesian sampling, it has been well known that this sampling lattice is sub-optimal. Yet, only recently advances have been made by introducing reconstruction filters for the 2D optimal lattice (e.g. the Hexagonal lattice). Our paper introduces novel reconstruction filters for the Body Centered Cubic (BCC) lattice, the analogous optimal sampling lattice in 3D, that are based on the geometric structure of the underlying lattice. This should pave the way for a more mainstream adaption of the BCC lattice for the discrete representation and processing of three dimensional phenomena.

An introduction to multi-dimensional sampling theory can be found in Dudgeon and Mersereau [5]. A lattice can be viewed as a periodic sampling pattern. Periodic sampling of a function in the spatial domain gives rise to a periodic replication of the spectrum in the Fourier domain. The lattice that describes the centers of the replicas in the Fourier domain is called the *dual*, *reciprocal*, or *polar* lattice. Reconstruction in the spatial domain amounts to eliminating the replicas of the spectrum in the Fourier domain while preserving the primary spectrum. Therefore, the ideal reconstruction function is the inverse Fourier transform of the characteristic function of the Voronoi cell of the dual lattice.

In Section 2 we will give a rigorous introduction to multidimensional sampling theory and derive the relationship between the sampling pattern in the spatial and the frequency domain. This will allow us to derive the notion of the optimal sampling lattice in Section 3. Section 4 will discuss and derive geometric aspects of the BCC and the FCC lattices, setting the stage for deriving nearest neighbor, linear and cubic reconstruction filters in Section 5. A practical implementation of the linear reconstruction filter is derived in Section 6 and Section 7 discusses our experimental evaluation. Finally, Section 8 and Section 9 summarize our contributions and point to some open problems, respectively.

2 Multidimensional Sampling Theory

Let $f \in L_2(\mathbb{R}^n)$ be a multivariate function for which the Fourier transform exists and let $\hat{f} : \mathbb{R}^n \to \mathbb{C}$ be its Fourier transform:

$$\hat{f}(\boldsymbol{\omega}) = \int f(\boldsymbol{x}) e^{-2\pi i \boldsymbol{\omega} \cdot \boldsymbol{x}} d\boldsymbol{x}$$

Given the fact that $\hat{f} \in L_2(\mathbb{R}^n)$ also, the inversion formula

$$f(\boldsymbol{x}) = \int \hat{f}(\boldsymbol{\omega}) e^{2\pi i \boldsymbol{\omega} \cdot \boldsymbol{x}} d\boldsymbol{\omega}$$

recovers the original function f almost everywhere [1]. If the original function is also continuous, the reconstruction equality holds everywhere [8].

We are interested in the regular sampling of a function and its reconstruction from the discrete set of samples. In this paper we shall refer to reconstruction in the space of functions with a compact support in their Fourier representations (i.e. bandlimited functions).

[1] Reconstruction takes the mean value of the left and the right limit at the points of discontinuity.

The sampling operation is defined over the space of square integrable functions ($L_2(\mathbb{R})$) equipped with the usual inner product:

$$\langle f, g \rangle = \int f(\boldsymbol{x}) g(\boldsymbol{x}) d\boldsymbol{x}.$$

Assuming sample values are produced by a sampling device which is characterized by a function, g, called its impulse response[2]. The sampling operation, takes a function that is an element of L_2 and returns a number. This operation can be modeled by the following functional:

$$L_2 \mapsto \mathbb{R} : f \mapsto \langle f, g \rangle .$$

The ideal impulse response (i.e. sampling function) is referred to as Dirac's delta (generalized) function which is the point evaluation functional defined by the following functional equation:

$$\delta[f] = f(0) \tag{1}$$

for all continuous functions f. Formally this symbol in an integral behaves as the limit of integrals of a sequence of integrable functions K_r that have the properties:

$$\int K_r(\boldsymbol{x}) d\boldsymbol{x} = 1 \text{ for all } r > 0$$
$$\lim_{r \to 0} K_r(\boldsymbol{x}) = 0 \text{ for all } \boldsymbol{x} \neq 0.$$

Examples of such kernels consist of Dirichlet, Fejér, Gaussian and Poisson kernels. It is customary to say that in the limit these kernels behave like the delta function:

$$\delta[f] = \lim_{r \to 0} \int K_r(\boldsymbol{x}) f(\boldsymbol{x}) d\boldsymbol{x} = f(0)$$

for all continuous functions f. Therefore the behavior of the functional in Equation 1 can be considered as the behavior of the above limit. As a notational convenience, the operation of δ on a function f is defined as:

$$\int \delta(\boldsymbol{x}) f(\boldsymbol{x}) d\boldsymbol{x} \triangleq \delta[f]$$

even though, such a function $\delta(\boldsymbol{x})$ does not exist. Since Dirac's generalized function is not a function in the classical setting, the symbolic introduction of Dirac's delta function is merely for the ease of notation.

A regular sampling pattern can be viewed as a point lattice. An n-dimensional *point lattice* is characterized by a set of n basis vectors $\{\boldsymbol{T_j}\}_{1 \leq j \leq n}$.

[2]In the medical imaging community the impulse response is sometimes referred to as the excitation function.

A point is on the lattice if and only if it is described by a linear combination with integer coefficients of the basis vectors. The matrix, $\boldsymbol{T} = [\boldsymbol{T}_1\boldsymbol{T}_2 \ldots \boldsymbol{T}_n]$, whose columns are the basis vectors is called the *sampling matrix* and any lattice point $\boldsymbol{t}$ is given by $\boldsymbol{t} = \boldsymbol{T}\boldsymbol{p}$ for some $\boldsymbol{p} \in \mathbb{Z}^n$. Figure 2 illustrates a two-dimensional lattice. The impulse response of such a sampling lattice is:

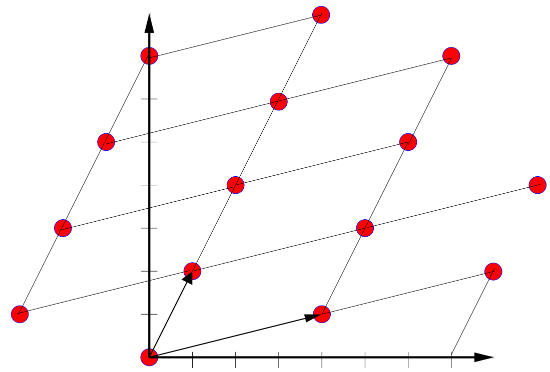

Fig. 1. A two-dimensional lattice with $\boldsymbol{T} = [\boldsymbol{T}_1\boldsymbol{T}_2]$, where $\boldsymbol{T}_1 = [4,1]^\top$ and $\boldsymbol{T}_2 = [1,2]^\top$.

$$\text{Ш}_{\boldsymbol{T}}(\boldsymbol{x}) = \sum_{\boldsymbol{k}\in\mathbb{Z}^n} \delta(\boldsymbol{x} - \boldsymbol{T}\boldsymbol{k}) \tag{2}$$

This equation is again a symbolic equation that eases the notation. The corresponding definition, then, is:

$$\int \text{Ш}_{\boldsymbol{T}}(\boldsymbol{x}) f(\boldsymbol{x}) d\boldsymbol{x} \triangleq \lim_{r\to 0} \int \sum_{\boldsymbol{k}\in\mathbb{Z}^n} K_r(\boldsymbol{x} - \boldsymbol{T}\boldsymbol{k}) f(\boldsymbol{x}) d\boldsymbol{x} \tag{3}$$

for all continuous functions f with bounded support.
The corresponding functional that defines the $\text{Ш}_{\boldsymbol{T}}$ is:

$$\int \text{Ш}_{\boldsymbol{T}}(\boldsymbol{x}) f(\boldsymbol{x}) d\boldsymbol{x} = \sum_{\boldsymbol{k}\in\mathbb{Z}^n} f(\boldsymbol{T}\boldsymbol{k}) \tag{4}$$

Therefore the function that is obtained by the sampling device is:

$$f_s(\boldsymbol{x}) = \text{Ш}_{\boldsymbol{T}}(\boldsymbol{x}) f(\boldsymbol{x}) \tag{5}$$

We observe that $\text{Ш}_{\boldsymbol{T}}$ is a periodic function with period $\boldsymbol{T}$: $\text{Ш}_{\boldsymbol{T}}(\boldsymbol{x} + \boldsymbol{T}\boldsymbol{m}) = \text{Ш}_{\boldsymbol{T}}(\boldsymbol{x})$ for $\boldsymbol{m} \in \mathbb{Z}^n$.

In order to study the effect of the sampling operator on the Fourier representation of the underlying function, we need to derive the Fourier transform (FT) of $\text{Ш}_{\boldsymbol{T}}$. Without claiming any of the convergence properties of the Fourier transform for the shah function, we transform the shah as:

$$\hat{\text{III}}_{\boldsymbol{T}}(\boldsymbol{\omega}) = \int \text{III}_{\boldsymbol{T}}(\boldsymbol{x}) e^{-2\pi i \boldsymbol{\omega}\cdot\boldsymbol{x}} d\boldsymbol{x}.$$

Since the exponential functions are continuous, Equation 4 yields:

$$\hat{\text{III}}_{\boldsymbol{T}}(\boldsymbol{\omega}) = \sum_{\boldsymbol{k}\in\mathbb{Z}^n} e^{-2\pi i \boldsymbol{\omega}\cdot(\boldsymbol{T}\boldsymbol{k})}.$$

Note that $\hat{\text{III}}_{\boldsymbol{T}}$ is periodic with the periodicity matrix $\tilde{\boldsymbol{T}} = \boldsymbol{T}^{-\top}$, since for any $\boldsymbol{m} \in \mathbb{Z}^n$:

$$\begin{aligned}
\hat{\text{III}}_{\boldsymbol{T}}(\boldsymbol{\omega} + \boldsymbol{T}^{-\top}\boldsymbol{m}) &= \sum_{\boldsymbol{k}\in\mathbb{Z}^n} e^{-2\pi i (\boldsymbol{\omega}+\boldsymbol{T}^{-\top}\boldsymbol{m})\cdot(\boldsymbol{T}\boldsymbol{k})} \\
&= \sum_{\boldsymbol{k}\in\mathbb{Z}^n} e^{-2\pi i \left[\boldsymbol{\omega}\cdot(\boldsymbol{T}\boldsymbol{k}) + (\boldsymbol{T}^{-\top}\boldsymbol{m})\cdot(\boldsymbol{T}\boldsymbol{k})\right]} \\
&= \sum_{\boldsymbol{k}\in\mathbb{Z}^n} e^{-2\pi i \left[\boldsymbol{\omega}\cdot(\boldsymbol{T}\boldsymbol{k}) + (\boldsymbol{m}^{\top}\boldsymbol{T}^{-1}\boldsymbol{T}\boldsymbol{k})\right]} \\
&= \sum_{\boldsymbol{k}\in\mathbb{Z}^n} e^{-2\pi i \left[\boldsymbol{\omega}\cdot(\boldsymbol{T}\boldsymbol{k}) + (\boldsymbol{m}^{\top}\boldsymbol{k})\right]} \\
&= \sum_{\boldsymbol{k}\in\mathbb{Z}^n} e^{-2\pi i \boldsymbol{\omega}\cdot(\boldsymbol{T}\boldsymbol{k})} e^{-2\pi i \boldsymbol{m}\cdot\boldsymbol{k}} \\
&= \sum_{\boldsymbol{k}\in\mathbb{Z}^n} e^{-2\pi i \boldsymbol{\omega}\cdot(\boldsymbol{T}\boldsymbol{k})} \text{ since } e^{-2\pi i \boldsymbol{m}\cdot\boldsymbol{k}} = 1 \text{ for all } \boldsymbol{m}, \boldsymbol{k} \in \mathbb{Z}^n \\
&= \hat{\text{III}}_{\boldsymbol{T}}(\boldsymbol{\omega}).
\end{aligned}$$

Theorem 1. *The Fourier transform of a Shah function $\text{III}_{\boldsymbol{T}}(\boldsymbol{x})$ over a lattice $\boldsymbol{T}$ as defined in Equation 2 can be described as another Shah function $\text{III}_{\tilde{\boldsymbol{T}}}(\boldsymbol{\omega})$ over the dual lattice $\tilde{\boldsymbol{T}} = \boldsymbol{T}^{-\top}$ with $\hat{\text{III}}_{\boldsymbol{T}}(\boldsymbol{\omega}) = \text{III}_{\tilde{\boldsymbol{T}}}(\boldsymbol{\omega})$*

Proof. To prove this theorem we note that the $\hat{\text{III}}_{\boldsymbol{T}}$ is $\tilde{\boldsymbol{T}}$ periodic. Let $\boldsymbol{\Omega} = \tilde{\boldsymbol{T}}[-\frac{1}{2}, \frac{1}{2})^n$ be one period of the domain $\mathbb{R}^n$. Therefore, all we need to show is that:

$$\int_{\boldsymbol{\Omega}} \hat{\text{III}}_{\boldsymbol{T}}(\boldsymbol{\omega}) g(\boldsymbol{\omega}) d\boldsymbol{\omega} = g(0) = \int \delta(\boldsymbol{\omega}) g(\boldsymbol{\omega}) d\boldsymbol{\omega} \tag{6}$$

for all continuous $g : \mathbb{R}^n \mapsto \mathbb{C}$ with bounded support.

For the choice of the kernel K_r in Equation 3, we resort to the Poisson kernel. The family of functions $P_r : \mathbb{R}^n \mapsto \mathbb{C}$, $0 < r < 1$ defined by:

$$P_r(\boldsymbol{\omega}) = \sum_{\boldsymbol{k}\in\mathbb{Z}^n} r^{\|\boldsymbol{k}\|} e^{2\pi i \boldsymbol{\omega}\cdot(\boldsymbol{T}\boldsymbol{k})}$$

where $\|\boldsymbol{k}\| = \sum_{i=1}^n |k_i|$ for $\boldsymbol{k} = [k_1 \ldots k_n]^\top$.

Expanding the right hand side of the above equation we have:

$$
\begin{aligned}
P_r(\tilde{\boldsymbol{T}}\boldsymbol{\omega}) &= \sum_{\boldsymbol{k}\in\mathbb{Z}^n} r^{\|\boldsymbol{k}\|} e^{2\pi i \boldsymbol{\omega}\cdot\boldsymbol{k}} \\
&= \sum_{k_1,k_2,\ldots,k_n\in\mathbb{Z}} r^{|k_1|} r^{|k_2|}\ldots r^{|k_n|} e^{2\pi i\omega_1 k_1} e^{2\pi i\omega_2 k_2}\ldots e^{2\pi i\omega_n k_n} \\
&= (\sum_{k_1\in\mathbb{Z}} r^{|k_1|} e^{2\pi i\omega_1 k_1})(\sum_{k_2\in\mathbb{Z}} r^{|k_2|} e^{2\pi i\omega_2 k_2})\ldots(\sum_{k_n\in\mathbb{Z}} r^{|k_n|} e^{2\pi i\omega_n k_n}) \\
&= P_r(\omega_1)P_r(\omega_2)\ldots P_r(\omega_n)
\end{aligned}
$$

In other words, the multi-dimensional Poisson kernel is a separable kernel and therefore we can use the following one-dimensional results from [1]:

$$
\begin{aligned}
&P_r(\omega) = \sum_{k\in\mathbb{Z}} r^{|k|} e^{2\pi i\omega k} \\
&P_r(\omega) \geq 0 \\
&\int_{[-\frac{1}{2},\frac{1}{2})} P_r(\omega)d\omega = 1
\end{aligned}
$$

Furthermore,[1]:

$$
\lim_{r\to 1}\int P_r(\omega)g(\omega)d\omega = g(0) = \int \delta(\omega)g(\omega)d\omega
$$

Since $P_r(\omega)$ is positive and bounded, $P_r(\boldsymbol{\omega}) \geq 0$ and by the Fubini theorem we have:

$$
\int_{[-\frac{1}{2},\frac{1}{2})^n} P_r(\tilde{\boldsymbol{T}}\boldsymbol{\omega})d\boldsymbol{\omega} = \int_{-\frac{1}{2}}^{\frac{1}{2}} P_r(\omega_1)d\omega_1 \int_{-\frac{1}{2}}^{\frac{1}{2}} P_r(\omega_2)d\omega_2 \ldots \int_{-\frac{1}{2}}^{\frac{1}{2}} P_r(\omega_n)d\omega_n = 1.
$$

Moreover, for any continuous function $g : \mathbb{R}^n \mapsto \mathbb{C}$ we have:

$$
\begin{aligned}
&\lim_{r\to 1}\int_{\boldsymbol{\Omega}} P_r(\boldsymbol{\omega})g(\boldsymbol{\omega})d\boldsymbol{\omega} = \\
&\qquad = \lim_{r\to 1}\int_{\omega_1}\ldots\int_{\omega_n} P_r(\omega_1,\ldots,\omega_n)g(\omega_1,\ldots,\omega_n)d\omega_n\ldots d\omega_1 \\
&\qquad = \lim_{r\to 1}\int_{\omega_1}\ldots\int_{\omega_{n-1}} P_r(\omega_1,\ldots,\omega_{n-1})g(\omega_1,\ldots,\omega_{n-1},0)d\omega_{n-1}\ldots d\omega_1 \\
&\qquad \vdots \\
&\qquad = \lim_{r\to 1}\int_{\omega_1} P_r(\omega_1)g(\omega_1,0,\ldots,0)d\omega_1 = g(0)
\end{aligned}
$$

Hence, we conclude by the dominated convergence theorem that:

$$
\lim_{r\to 1}\int_{\boldsymbol{\Omega}} P_r(\boldsymbol{\omega})g(\boldsymbol{\omega})d\boldsymbol{\omega} = \int_{\boldsymbol{\Omega}} \hat{\text{III}}_{\boldsymbol{T}}(\boldsymbol{\omega})g(\boldsymbol{\omega})d\boldsymbol{\omega} = g(0)
$$

Since $\hat{Ш}_{\boldsymbol{T}}$ is $\tilde{\boldsymbol{T}}$ periodic, we have:

$$\hat{Ш}_{\boldsymbol{T}}(\boldsymbol{\omega}) = Ш_{\tilde{\boldsymbol{T}}}(\boldsymbol{\omega}).$$

This equality is again a symbolic equality and its meaning is only defined under an integral:

$$\int \hat{Ш}_{\boldsymbol{T}}(\boldsymbol{\omega}) f(\boldsymbol{\omega}) d\boldsymbol{\omega} = \int Ш_{\tilde{\boldsymbol{T}}}(\boldsymbol{\omega}) f(\boldsymbol{\omega}) d\boldsymbol{\omega} \tag{7}$$

for all continuous functions f with bounded support.

In conclusion, the Fourier transform of $Ш_{\boldsymbol{T}}$ is yet another shah function on the reciprocal lattice $Ш_{\tilde{\boldsymbol{T}}}$. $\square$

In order to find the Fourier transform of the sampled function f_s as in Equation 5, one can use the Convolution-Multiplication theorem to show:

$$\hat{f}_s(\boldsymbol{\omega}) = (\hat{Ш}_{\boldsymbol{T}} * \hat{f})(\boldsymbol{\omega}) = (Ш_{\tilde{\boldsymbol{T}}} * \hat{f})(\boldsymbol{\omega})$$

The important observation from this result is that the two lattices represented by $\boldsymbol{T}$ and $\tilde{\boldsymbol{T}}$ are duals of each other through the Fourier transform.

3 The Optimal Lattice Sampling

The main result of the previous section was that sampling a function f on a lattice $\boldsymbol{T}$, brings about the replication of the Fourier Transform of f on the dual lattice $\tilde{\boldsymbol{T}} = \boldsymbol{T}^{-\top}$. Due to this reciprocal relationship, the sparsest sampling matrix $\boldsymbol{T}$ will have to produce the densest packing of the replicas of the spectrum on the dual lattice $\tilde{\boldsymbol{T}}$. Therefore, in order to distribute the samples in the spatial domain in the most economical (sparse) fashion, the dual lattice $\tilde{\boldsymbol{T}}$ needs to be as densely packed as possible.

In the typical three-dimensional case, usually there is no knowledge of a direction of preferred resolution for sampling the underlying function f and the function is assumed to be qualitatively isotropic. This means that f has a spherically uniform spectrum. With this assumption, the dense packing of the spectra in the Fourier domain can be addressed by the sphere packing problem. Consequently the best sampling lattice in 3D is dual to the lattice that attains the highest sphere packing density.

The sphere packing problem [3] can be traced back to the early 17th century . Finding the densest packing of spheres is known as the Kepler problem. The fact that the face centered cubic (FCC) packing attains the highest density of lattice packings was first proven by Gauß in 1831 [3]. Further, the Kepler conjecture – that the FCC packing is an optimal packing of spheres in 3D even when the lattice condition is not imposed – was not proven until 1998 by a lengthy computer-aided proof [6].

In two dimensions however, the hexagonal packing structure can be easily shown to attain the optimal density of packing. Since the two dimensional hexagonal lattice is self-dual, the optimal sampling in 2D is a hexagonal lattice. Consequently, by sampling a 2D function f on a hexagonal lattice, its Fourier domain representation is replicated on the dual hexagonal lattice; similarly by sampling a function on the commonly used Cartesian lattice, its Fourier domain representation is replicated on the dual Cartesian lattice.

Figure 2 illustrates the optimality of hexagonal sampling versus Cartesian sampling. An equivalent spatial domain sampling density is used for both the Cartesian and the hexagonal sampling lattice. The Fourier domain replication is shown for the Cartesian lattice in Figure 2(a) and for the hexagonal lattice in Figure 2(b). It is apparent that the area of the main spectrum (in red) that is captured in the hexagonal case is larger than that of the Cartesian case. This means that with the equivalent sampling density in the spatial domain, the hexagonal sampling captures more of the frequency content of the spectrum of f and in the process of band limiting the underlying signal for sampling, we can allow a larger baseband to be captured. This means that more information can be captured with the same number of samples. The increased efficiency of the optimal sampling lattice in 2D is about 14% and in 3D it is about 30%.

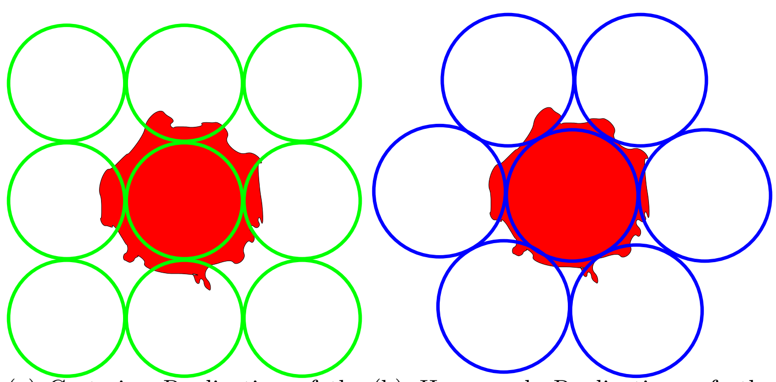

(a) Cartesian Replication of the Spectrum

(b) Hexagonal Replication of the Spectrum

Fig. 2. Hexagonal sampling captures higher frequencies with equal sampling density

While the optimal regular sampling theory is attractive for its theoretical advantages, it hasn't been widely employed in practice due to the lack of signal processing theory and tools to handle such a sampling lattice.

4 The BCC Lattice

A *lattice* can be viewed as an infinite array of points in which each point has surroundings identical to those of all the other points [2]. In other words, every lattice point has the same Voronoi cell and we can refer to the Voronoi cell of the lattice without ambiguity. The lattice points form a group under vector addition in the Euclidean space.

The BCC lattice is a sub-lattice of the Cartesian lattice. The BCC lattice points are located on the corners of the cube with an additional sample in the center of the cube as illustrated in Figure 3. An alternative way of describing the BCC lattice is to start with a Cartesian lattice (i.e. $\mathbb{Z}^3$) and retain only those points whose coordinates have identical parity.

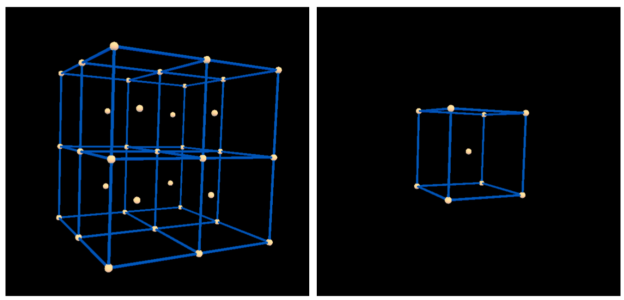

(a) (b)

Fig. 3. The BCC Lattice. A neighborhood of 35 points is displayed on the left, while a simple neighborhood of 9 points is displayed on the right.

The simplest interpolation kernel on any lattice is the characteristic function of the Voronoi cell of the lattice. This is usually called nearest neighbor interpolation. More sophisticated reconstruction kernels involve information from the neighboring points of a given lattice point. With this in mind, we focus in the next section on the geometry and the polyhedra associated with the BCC lattice.

4.1 Polyhedra Associated with the BCC Lattice

Certain polyhedra arise naturally in the process of constructing interpolation filters for a lattice. The Voronoi cell of the lattice is one such example. The Voronoi cell of the Cartesian lattice is a cube and the Voronoi cell of the BCC lattice is a truncated octahedron as illustrated in Figure 4a.

We are also interested in the cell formed by the immediate neighbors of a lattice point. The first neighbors of a lattice point are defined by the Delaunay tetrahedralization of the lattice; a point $\boldsymbol{q}$ is a *first neighbor* of $\boldsymbol{p}$ if their respective Voronoi cells share a (non-degenerate) face. The *first neighbors cell* is the polyhedron whose vertices are the first neighbors. Again, this cell is the same for all points on the lattice.

For example, by this definition there are six first neighbors of a point in a Cartesian lattice; the first neighbors cell for the Cartesian lattice is the octahedron. For the BCC lattice there are fourteen first neighbors for each lattice point. The first neighbor cell is a rhombic dodecahedron as illustrated in Figure 4b.

The geometry of the dual lattice is of interest when we consider the spectrum of the function captured by the sampling operation. The Cartesian lattice is self dual. However, the dual of the BCC lattice is the FCC lattice. The FCC lattice is a sublattice of $\mathbb{Z}^3$ and is often referred to as the $\boldsymbol{D}_3$ lattice [3]. In fact $\boldsymbol{D}_3$ belongs to a general family of lattices, $\boldsymbol{D}_n$, sometimes called checkerboard lattices. The checkerboard property implies that the sum of the coordinates of the lattice sites is always even. We will use this property to demonstrate the zero crossings of the frequency response of the reconstruction filters at the FCC lattice sites.

The Voronoi cell of the FCC lattice is the rhombic dodecahedron as illustrated in Figure 4c. Its characteristic function is the frequency response of the ideal reconstruction filter for the BCC lattice. Figure 4d shows the first neighbors cell of the FCC lattice; the cuboctahedron.

5 Reconstruction Filters

The kernel for the nearest neighbor interpolation in 1D is the Box function. It is the characteristic function of the Voronoi cell of the samples on the real line. The nearest neighbor interpolation on the BCC lattice is similarly defined in terms of the Voronoi cell of the lattice which is a truncated octahedron (Figure 4(a)). In this scheme, a point in space is assigned the value of the sample in whose Voronoi cell it is located. Since the Voronoi cell tiles the space, its characteristic function induces an interpolation scheme for that lattice. Based on the fact that the periodic tiling of the Voronoi cell yields the constant function in the spatial domain, Van De Ville [12] proves by means of the Poisson summation formula that the frequency response of such a kernel does in fact vanish at the aliasing frequencies.

5.1 Ideal Interpolation

As noted earlier, sampling a function on a periodic lattice replicates the spectrum of the function in the Fourier domain on the dual lattice. When the space of bandlimited functions is the space of choice for reconstruction, the ideal interpolation function is the one that removes the replicates of the spectrum in the Fourier domain. This proves that the Fourier transform of the ideal interpolation function is the characteristic function of the Voronoi cell of the

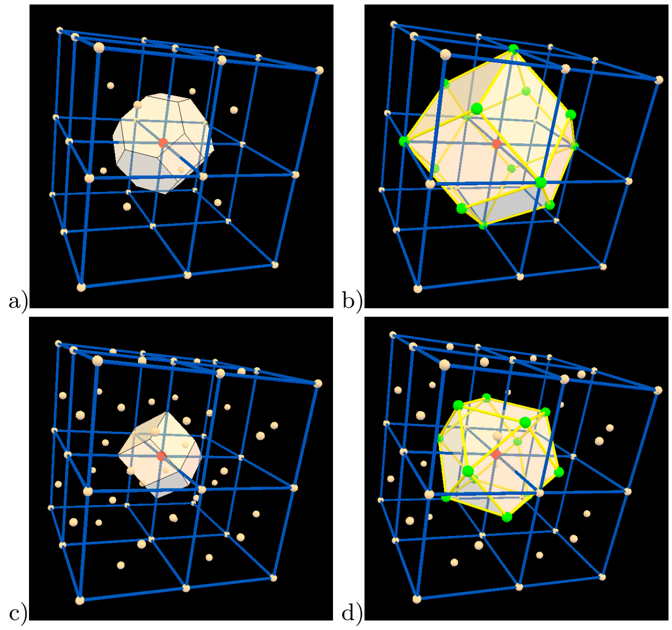

Fig. 4. The Voronoi cell of the BCC lattice is the truncated octahedron (a), and its first neighbor cell is the rhombic dodecahedron (b). For the FCC lattice, the rhombic dodecahedron is the Voronoi cell (c), and the cuboctahedron is the first neighbor cell (d).

dual lattice; hence, convolving by the ideal interpolation function, leaves out the main spectrum and eliminates all of the replicas.

The ideal reconstruction function for the Cartesian lattice has a Fourier transform that is the characteristic function of a cube and the one for the BCC lattice has Fourier transform which is the characteristic function of a rhombic dodecahedron. Therefore, in order to find the ideal interpolation function for the BCC lattice we need to find a function whose Fourier transform is constant on the rhombic dodecahedron in Figure 4(c) and is zero everywhere else.

As it is not easy to derive this function directly, to construct an explicit function we decompose the rhombic dodecahedron into simpler objects that are easy to construct in the dual domain. Figure 5 illustrates the decomposition of the rhombic dodecahedron into four three dimensional parallelepipeds. These parallelepipeds share the origin and each are formed by three vectors from the origin. For a rhombic dodecahedron oriented as in Figure 4(c) we define the set of vectors:

$$\boldsymbol{\xi}_1 = \begin{bmatrix} -1 \\ -1 \\ 1 \end{bmatrix}, \boldsymbol{\xi}_2 = \begin{bmatrix} -1 \\ 1 \\ -1 \end{bmatrix}, \boldsymbol{\xi}_3 = \begin{bmatrix} 1 \\ -1 \\ -1 \end{bmatrix}, \boldsymbol{\xi}_4 = \begin{bmatrix} 1 \\ 1 \\ 1 \end{bmatrix}.$$

Any three of these four vectors form one of the parallelepipeds in the decomposition of the rhombic dodecahedron illustrated in Figure 5. One can observe that:

$$\boldsymbol{\xi}_1 + \boldsymbol{\xi}_2 + \boldsymbol{\xi}_3 + \boldsymbol{\xi}_4 = \begin{bmatrix} 0 \\ 0 \\ 0 \end{bmatrix} \tag{8}$$

that is attributed to the symmetries of the rhombic dodecahedron.

Since a parallellepiped can be constructed by a linear transform from a cube, we can start by constructing a cube in the Fourier domain:

$$\mathcal{F}\{\operatorname{sinc}(x)\operatorname{sinc}(y)\operatorname{sinc}(z)\} = \mathcal{B}(\omega_x)\,\mathcal{B}(\omega_y)\,\mathcal{B}(\omega_z)$$

where $\operatorname{sinc}(x) = \frac{\sin(\pi x)}{\pi x}$. Rewriting the above equation in terms of a 3D extension of sinc:

$$\mathcal{F}\{\operatorname{sinc}_{3D}(\boldsymbol{x})\} = \mathcal{B}_{3D}(\boldsymbol{\omega}).$$

Let $\boldsymbol{\xi}_i, \boldsymbol{\xi}_j, \boldsymbol{\xi}_k$ denote the vectors forming a parallelepiped. Then the matrix $\boldsymbol{T} = [\boldsymbol{\xi}_i|\boldsymbol{\xi}_j|\boldsymbol{\xi}_k]$ transforms the unit cube to the parallelepiped. If $\chi_{\boldsymbol{T}}$ denotes the characteristic function of the parallelepiped formed by the columns of $\boldsymbol{T}$, then:

$$\chi_{\boldsymbol{T}}(\boldsymbol{\omega}) = \mathcal{B}_{3D}(\boldsymbol{T}^{-1}\boldsymbol{\omega}).$$

In order to get $\chi_{\boldsymbol{T}}$ in the Fourier domain, we use the multidimensional scaling lemma in the Fourier transform:

$$\mathcal{F}\{\operatorname{sinc}_{3D}(\boldsymbol{T}^{\top}\boldsymbol{x})\} = \det \boldsymbol{T}\chi_{\boldsymbol{T}}(\boldsymbol{\omega}).$$

That means the spatial domain form of a constant parallelpiped formed by $\boldsymbol{T}$ in the Fourier domain is:

$$\mathcal{F}\{\operatorname{sinc}(\boldsymbol{\xi}_i \cdot \boldsymbol{x})\operatorname{sinc}(\boldsymbol{\xi}_j \cdot \boldsymbol{x})\operatorname{sinc}(\boldsymbol{\xi}_k \cdot \boldsymbol{x})\} = \det \boldsymbol{T}\chi_{\boldsymbol{T}}(\boldsymbol{\omega}). \tag{9}$$

This equation represents a parallelepiped that is centered at the origin; in order to represent the parallelepipeds in Figure 5 we need to shift them so that the origin is at the corner of each parallelepiped. The shift is along the antipodal diagonal of the parallelepiped by half the length of the antipodal diagonal. The shift in the Fourier domain can be achieved by a phase shift in the space domain. Therefore, the space domain representation of a parallelepiped formed by $\boldsymbol{T}$ with its corner at the origin is

$$\mathcal{F}\{e^{-2\pi i\frac{1}{2}(\boldsymbol{\xi}_i+\boldsymbol{\xi}_j+\boldsymbol{\xi}_k)\cdot\boldsymbol{x}}\operatorname{sinc}(\boldsymbol{\xi}_i \cdot \boldsymbol{x})\operatorname{sinc}(\boldsymbol{\xi}_j \cdot \boldsymbol{x})\operatorname{sinc}(\boldsymbol{\xi}_k \cdot \boldsymbol{x})\} = \det \boldsymbol{T}\chi^o_{\boldsymbol{T}}(\boldsymbol{\omega}).$$

where $\chi^o_{\boldsymbol{T}}$ is the characteristic function of the parallelepiped with its corner at the origin.

Now we can write the space domain representation of the rhombic dodecahedron in Figure 4(c).

$$
\begin{aligned}
\mathrm{sincBCC}(\boldsymbol{x}) = & \\
& e^{\pi i \boldsymbol{\xi}_4 \cdot \boldsymbol{x}} \,\mathrm{sinc}(\boldsymbol{\xi}_1 \cdot \boldsymbol{x})\,\mathrm{sinc}(\boldsymbol{\xi}_2 \cdot \boldsymbol{x})\,\mathrm{sinc}(\boldsymbol{\xi}_3 \cdot \boldsymbol{x}) + \\
& e^{\pi i \boldsymbol{\xi}_3 \cdot \boldsymbol{x}} \,\mathrm{sinc}(\boldsymbol{\xi}_1 \cdot \boldsymbol{x})\,\mathrm{sinc}(\boldsymbol{\xi}_2 \cdot \boldsymbol{x})\,\mathrm{sinc}(\boldsymbol{\xi}_4 \cdot \boldsymbol{x}) + \\
& e^{\pi i \boldsymbol{\xi}_2 \cdot \boldsymbol{x}} \,\mathrm{sinc}(\boldsymbol{\xi}_1 \cdot \boldsymbol{x})\,\mathrm{sinc}(\boldsymbol{\xi}_3 \cdot \boldsymbol{x})\,\mathrm{sinc}(\boldsymbol{\xi}_4 \cdot \boldsymbol{x}) + \\
& e^{\pi i \boldsymbol{\xi}_1 \cdot \boldsymbol{x}} \,\mathrm{sinc}(\boldsymbol{\xi}_2 \cdot \boldsymbol{x})\,\mathrm{sinc}(\boldsymbol{\xi}_3 \cdot \boldsymbol{x})\,\mathrm{sinc}(\boldsymbol{\xi}_4 \cdot \boldsymbol{x}) \\
= & \sum_{j=1}^{4} e^{\pi i \boldsymbol{\xi}_j \cdot \boldsymbol{x}} \prod_{k \neq j} \mathrm{sinc}(\boldsymbol{\xi}_k \cdot \boldsymbol{x}).
\end{aligned}
\tag{10}
$$

Claim. $\mathrm{sincBCC}(\boldsymbol{x})$ is a real valued function

Proof. In order to show that $\mathrm{sincBCC}(\boldsymbol{x})$ is a real valued function we subtract it from its conjugate:

$$
\begin{aligned}
& \overline{\mathrm{sincBCC}(\boldsymbol{x})} - \mathrm{sincBCC}(\boldsymbol{x}) = \\
& \sum_{j=1}^{4} (e^{-\pi i \boldsymbol{\xi}_j \cdot \boldsymbol{x}} - e^{\pi i \boldsymbol{\xi}_j \cdot \boldsymbol{x}}) \prod_{k \neq j} \mathrm{sinc}(\boldsymbol{\xi}_k \cdot \boldsymbol{x}) = \\
& \sum_{j=1}^{4} (2i \sin(\pi \boldsymbol{\xi}_j \cdot \boldsymbol{x})) \prod_{k \neq j} \mathrm{sinc}(\boldsymbol{\xi}_k \cdot \boldsymbol{x}) = \\
& \sum_{j=1}^{4} (2\pi i (\boldsymbol{\xi}_j \cdot \boldsymbol{x})\,\mathrm{sinc}(\boldsymbol{\xi}_j \cdot \boldsymbol{x})) \prod_{k \neq j} \mathrm{sinc}(\boldsymbol{\xi}_k \cdot \boldsymbol{x}) = \\
& \sum_{j=1}^{4} 2\pi i (\boldsymbol{\xi}_j \cdot \boldsymbol{x}) \prod \mathrm{sinc}(\boldsymbol{\xi}_k \cdot \boldsymbol{x}) = \\
& 2\pi i ((\boldsymbol{\xi}_1 + \boldsymbol{\xi}_2 + \boldsymbol{\xi}_3 + \boldsymbol{\xi}_4) \cdot \boldsymbol{x}) \prod \mathrm{sinc}(\boldsymbol{\xi}_k \cdot \boldsymbol{x}) = 0
\end{aligned}
$$

due to symmetries of the rhombic dodecahedron illustrated in Equation 8.

As a corollary to this claim, using the fact that $\mathrm{sincBCC}(\boldsymbol{x}) = \Re\{\mathrm{sincBCC}(\boldsymbol{x})\} = \frac{1}{2}(\mathrm{sincBCC}(\boldsymbol{x}) + \overline{\mathrm{sincBCC}(\boldsymbol{x})})$ we simplify the $\mathrm{sincBCC}(\boldsymbol{x})$ to :

$$
\mathrm{sincBCC}(\boldsymbol{x}) = \sum_{j=1}^{4} \cos(\pi \boldsymbol{\xi}_j \cdot \boldsymbol{x}) \prod_{k \neq j} \mathrm{sinc}(\boldsymbol{\xi}_k \cdot \boldsymbol{x}). \tag{11}
$$

5.2 Linear Box Spline

de Boor et al [4] analytically define the box splines, in n-dimensional space, by successive directional convolutions. They also describe an alternative geometric description of the box splines in terms of the projection of higher dimensional boxes (nD cubes). A simple example of a one dimensional linear

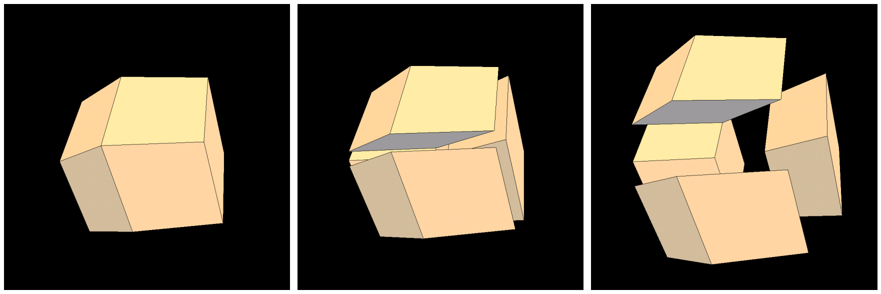

(a) (b) (c)

Fig. 5. The rhombic dodecahedron, the Voronoi cell of the FCC lattice, can be decomposed into four parallelpipeds.

box spline is the triangle function which can be obtained by projecting a 2D box along its diagonal axis down to 1D. The resulting function (after proper scaling) is one at the origin and has a linear fall off towards the first neighbors as illustrated in Figure 6a.

The properties and behaviors of box splines are studied in [4]. For example, the order of the box splines can be determined in terms of the difference in dimension between the higher dimensional box and the lower dimensional projection. For instance, the triangle function is a projection of a 2D cube into 1D, hence it is a first order box spline.

Our construction of box splines for the BCC lattice is guided by the fact that the rhombic dodecahedron (the first neighbors cell of the BCC lattice) is the three-dimensional shadow of a four-dimensional hypercube (tesseract) along its antipodal axis. This fact will be revealed in the following discussion. This construction is reminiscent of constructing a hexagon by projecting a three-dimensional cube along its antipodal axis; see Figure 6b for the 2D case.

Integrating a constant tesseract of unit side length along its antipodal axis yields a function that has a rhombic dodecahedron support (see Figure 3b), has the value two[3] at the center and has a linear fall off towards the fourteen first neighbor vertices. Since it arises from the projection of a higher dimensional box, this filter is the first order (linear) box spline interpolation filter on the BCC lattice.

Let $\mathcal{B}$ denote the Box distribution. The characteristic function of the unit tesseract is given by a product of these functions:

$$\mathcal{T}(x, y, z, w) = \mathcal{B}(x)\,\mathcal{B}(y)\,\mathcal{B}(z)\,\mathcal{B}(w). \tag{12}$$

Let $\boldsymbol{v} = \langle 1, 1, 1, 1\rangle$ denote a vector along the antipodal axis. In order to project along this axis, it is convenient to rotate it so that it aligns with the w axis.

[3]Note that the BCC sampling lattice has a sampling density of two samples per unit volume.

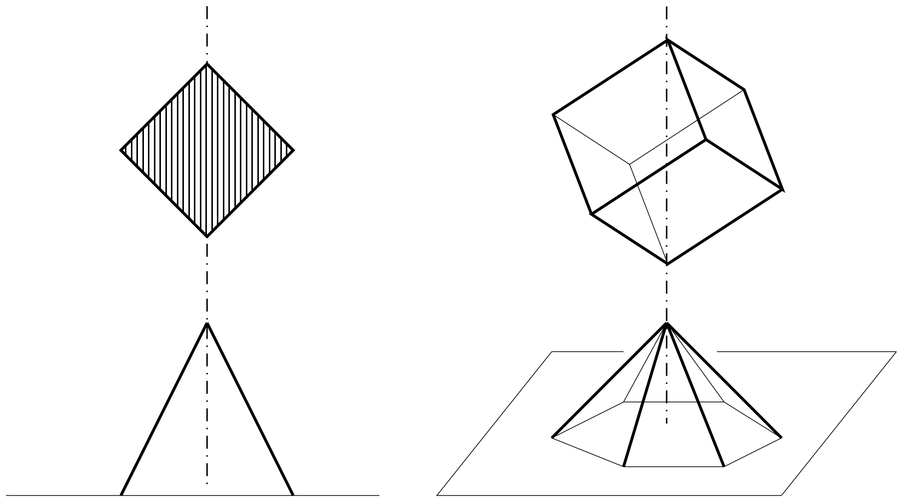

a b

Fig. 6. a) one dimensional linear box spline (Triangle function). b) the two dimensional hexagonal linear box spline

Let

$$\boldsymbol{R} = \frac{1}{2}[\boldsymbol{\rho}_1\boldsymbol{\rho}_2\boldsymbol{\rho}_3\boldsymbol{\rho}_4] = \frac{1}{2}\begin{bmatrix} -1 & -1 & 1 & 1 \\ -1 & 1 & -1 & 1 \\ 1 & -1 & -1 & 1 \\ 1 & 1 & 1 & 1 \end{bmatrix} \tag{13}$$

This rotation matrix transforms $\boldsymbol{v}$ to $\langle 0, 0, 0, 2\rangle$.[4] Let $\boldsymbol{x} = \langle x, y, z, w\rangle$; now the linear kernel is given by

$$L_{RD}(x, y, z) = \int \mathcal{T}(\boldsymbol{R}^\top \boldsymbol{x})\, dw.$$

Substituting in equation (12) we get

$$L_{RD}(x, y, z) = \int \prod_{i=1}^{4} \mathcal{B}(\frac{1}{2}\boldsymbol{\rho}_i \cdot \boldsymbol{x})\, dw. \tag{14}$$

We illustrate an analytical evaluation of this integral in Section 6.

5.3 Cubic Box Spline

By convolving the linear box spline filter kernel with itself we double its vanishing moments in the frequency domain. Hence the result of such an operation

[4]By examining equation (13), one can see that each vertex of the rotated tesseract, when projected along the w axis, will coincide with the origin or one of the vertices of the rhombic dodecahedron: $\left\langle \pm\frac{1}{2}, \pm\frac{1}{2}, \pm\frac{1}{2}\right\rangle$, $\langle \pm 1, 0, 0\rangle$, $\langle 0, \pm 1, 0\rangle$ or $\langle 0, 0, \pm 1\rangle$.

will have a cubic approximation order [11]. As noted by de Boor [4], the convolution of two box splines is again a box spline.

An equivalent method of deriving this function would be to convolve the tesseract with itself and project the resulting distribution along a diagonal axis (this commutation of convolution and projection is easy to understand in terms of the corresponding operators in the Fourier domain – see Section 5.4). Convolving a tesseract with itself results in another tesseract which is the tensor product of four one-dimensional triangle functions.

Let Λ denote the triangle function. Then convolving the characteristic function of the tesseract yields

$$\mathcal{T}_c(x, y, z, w) = \Lambda(x)\,\Lambda(y)\,\Lambda(z)\,\Lambda(w). \tag{15}$$

Following the same 4D rotation as in the previous section, we obtain a space domain representation of the cubic box spline filter kernel:

$$C_{RD}(x, y, z) = \int \prod_{i=1}^{4} \Lambda(\frac{1}{2}\boldsymbol{\rho}_i \cdot \boldsymbol{x})\, dw. \tag{16}$$

Again, we will illustrate in Section 6 how to evaluate this integral analytically.

5.4 Frequency Response

From the construction of the rhombic dodecahedron discussed earlier, we can analytically derive the frequency response of the linear function described by equation (14).

From equation (12), it is evident that the frequency domain representation of the characteristic function of the tesseract is given by the product of four sinc functions:

$$\tilde{\mathcal{T}}(\omega_x, \omega_y, \omega_z, \omega_w) = \operatorname{sinc}(\omega_x)\operatorname{sinc}(\omega_y)\operatorname{sinc}(\omega_z)\operatorname{sinc}(\omega_w).$$

While in the previous section the origin was assumed to be at the corner of the tesseract, for the simplicity of derivation, we now consider a tesseract whose center is at the origin. The actual integral, computed in Equation 14 or Equation 16 will not change.

By the Fourier slice-projection theorem, projecting the tesseract in the spatial domain is equivalent to slicing $\tilde{\mathcal{T}}$ perpendicular to the direction of projection. This slice runs through the origin. Again we make use of the rotation (13) to align the projection axis with the w axis. Thus in the frequency domain we take the slice $\omega_w = 0$.

It is convenient to introduce the 3×4 matrix

$$\boldsymbol{\Xi} = \frac{1}{2}[\boldsymbol{\xi}_1 \boldsymbol{\xi}_2 \boldsymbol{\xi}_3 \boldsymbol{\xi}_4] = \frac{1}{2}\begin{bmatrix} -1 & -1 & 1 & 1 \\ -1 & 1 & -1 & 1 \\ 1 & -1 & -1 & 1 \end{bmatrix} \tag{17}$$

given by the first three rows of the rotation matrix $\boldsymbol{R}$ of equation (13). The frequency response of the linear kernel can now be written as

$$\tilde{L}_{RD}(\omega_x, \omega_y, \omega_z) = \prod_{i=1}^{4} \operatorname{sinc}\left(\frac{1}{2}\boldsymbol{\xi}_i \cdot \boldsymbol{\omega}\right), \tag{18}$$

where $\boldsymbol{\omega} = \langle \omega_x, \omega_y, \omega_z \rangle$.

The box spline associated with this filter is represented by the $\boldsymbol{\Xi}$ matrix. The properties of this box spline can be derived based on this matrix according to the theory developed in [4]. For instance, one can verify C^0 smoothness of this filter using $\boldsymbol{\Xi}$.

We can verify the zero crossings of the frequency response at the aliasing frequencies on the FCC lattice points. Due to the checkerboard property for every $\boldsymbol{\omega}$ on the FCC lattice, $\boldsymbol{\xi}_4 \cdot \boldsymbol{\omega} = (\omega_x + \omega_y + \omega_z) = 2k$ for $k \in \mathbb{Z}$; therefore, $\operatorname{sinc}(\frac{1}{2}\boldsymbol{\xi}_4 \cdot \boldsymbol{\omega}) = 0$ on all of the aliasing frequencies. Since $\boldsymbol{\xi}_4 \cdot \boldsymbol{\omega} = -\boldsymbol{\xi}_1 \cdot \boldsymbol{\omega} - \boldsymbol{\xi}_2 \cdot \boldsymbol{\omega} - \boldsymbol{\xi}_3 \cdot \boldsymbol{\omega}$, at least one of the $\boldsymbol{\xi}_i \cdot \boldsymbol{\omega}$ for $i = 1, 2, 3$ needs to be also an even integer and for such i we have $\operatorname{sinc}(\frac{1}{2}\boldsymbol{\xi}_i \cdot \boldsymbol{\omega}) = 0$; therefore, there is a zero of order at least two at each aliasing frequency, yielding a C^0 filter.

The cubic box spline filter can be similarly derived by projecting a tesseract composed of triangle functions. Again, the frequency response can be obtained via the Fourier slice-projection theorem.

Since convolution corresponds to multiplication in the dual domain, the frequency response of (15) is

$$\tilde{\mathcal{T}}_c(\omega_x, \omega_y, \omega_z, \omega_w) = \operatorname{sinc}^2(\omega_x) \operatorname{sinc}^2(\omega_y) \operatorname{sinc}^2(\omega_z) \operatorname{sinc}^2(\omega_w).$$

By rotating and taking a slice as before we obtain:

$$\tilde{C}_{RD}(\omega_x, \omega_y, \omega_z) = \prod_{i=1}^{4} \operatorname{sinc}^2\left(\frac{1}{2}\boldsymbol{\xi}_i \cdot \boldsymbol{\omega}\right). \tag{19}$$

We can see that the vanishing moments of the cubic kernel are doubled from the linear kernel. We could also have obtained Equation 19 by simply multiplying Equation 18 with itself, which corresponds to convolving the linear 3D kernel with itself in the spatial domain.

The box spline matrix for the cubic kernel is $\boldsymbol{\Xi}' = [\boldsymbol{\Xi} | \boldsymbol{\Xi}]$. One can verify the C^2 continuity of this box spline using $\boldsymbol{\Xi}'$ and the theory in [4].

6 Implementation

In this section we describe a method to evaluate the linear and the cubic kernel analytically.

Let $\mathcal{H}$ denote the Heaviside distribution. Using the fact that $\mathcal{B}(x) = \mathcal{H}(x) - \mathcal{H}(x-1)$ we can expand the integrand of the linear kernel (Equation 14) in terms of Heaviside distributions. After simplifying the product of four Box distributions in terms of $\mathcal{H}$, we get sixteen terms in the integrand. Each term in the integrand is a product of four Heaviside distributions. Since x, y, z are constants in the integral and the integration is with respect to w, we group the x, y, z argument of each $\mathcal{H}$ and call it t_i, using the fact that $\mathcal{H}(\frac{1}{2}x) = \mathcal{H}(x)$, we can write each term in the integrand as:

$$I = \int_a^b \mathcal{H}(w + t_0)\,\mathcal{H}(w + t_1)\,\mathcal{H}(w + t_2)\,\mathcal{H}(w + t_3)\,dw.$$

The integrand is non-zero only when all of the Heaviside distributions are non-zero and since the integrand will be constant one we have:

$$I = \max(0, b - \max(a, \max(-t_i))).$$

Similarly, for the cubic kernel in Equation 16 we substitute $\Lambda(x) = \mathcal{R}(x) - 2\,\mathcal{R}(x-1) + \mathcal{R}(x-2)$, where $\mathcal{R}$ denotes the ramp function. We obtain eighty one terms, each of which is a product of four ramp functions. Using $\mathcal{R}(\frac{1}{2}x) = \frac{1}{2}\,\mathcal{R}(x)$, we can write each term in the integrand as a scalar fraction of:

$$I = \int_a^b \mathcal{R}(w + t_0)\,\mathcal{R}(w + t_1)\,\mathcal{R}(w + t_2)\,\mathcal{R}(w + t_3)\,dw.$$

This simplifies to a polynomial times four Heaviside distributions that we can evaluate analytically:

$$\begin{aligned} I &= \int_a^b \prod_{i=1}^{4} (w + t_i)\,\mathcal{H}(w + t_i)\,dw \\ &= \int_c^b \prod_{i=1}^{4} (w + t_i)\,dw. \end{aligned}$$

where $c = \min(b, \max(a, \max(-t_i)))$ and one can compute the integral of this polynomial analytically.

6.1 Simplification of the Linear Kernel

An alternative method of deriving the linear kernel can be obtained through a geometric argument.

All of the polyhedra discussed in Section 4 are convex and therefore may be described as the intersection of a set of half spaces. Further, each face is matched by a parallel antipodal face; this is due to the group structure of the lattice. If a point $\boldsymbol{a}$ is in the lattice and vector $\boldsymbol{b}$ takes it to a neighbor then $\boldsymbol{a} + \boldsymbol{b}$ is in the lattice; then the group property enforces $\boldsymbol{a} - \boldsymbol{b}$ be a point in the lattice as well, hence the antipodal symmetry. As a consequence the polyhedra lend themselves to a convenient description in terms of the level sets of piecewise linear functions.

Consider the rhombic dodecahedron, for example. Each of its twelve rhombic faces can be seen to lie centered on the edges of a cube such that the vector from the center of the cube to the center of its edge is orthogonal to the rhombic face placed on that edge.

So the interior of the rhombic dodecahedron that encloses the unit cube in this way can be described as the intersection of the twelve half spaces

$$\pm x \pm y \leq \sqrt{2}, \quad \pm x \pm z \leq \sqrt{2}, \quad \pm y \pm z \leq \sqrt{2}. \tag{20}$$

Now consider the pyramid with apex at the center of the polyhedron and whose base is a face f with unit outward normal $\hat{\boldsymbol{n}}_f$. Notice that for any point $\boldsymbol{p}$ within this pyramid, the scalar product $p \cdot \hat{\boldsymbol{n}}_f$ is larger than $p \cdot \hat{\boldsymbol{n}}_{f'}$, where $\hat{\boldsymbol{n}}_{f'}$ is the outward normal for any other rhombic face f'. Thus if we define a function

$$\begin{aligned} \phi &: \mathbb{R}^3 \longrightarrow \mathbb{R} \\ \phi &: \boldsymbol{p} \longmapsto \max_{\hat{\boldsymbol{n}}_f} p \cdot \hat{\boldsymbol{n}}_f, \end{aligned} \tag{21}$$

its level sets are rhombic dodecahedra. We can use the axial symmetries of the half spaces (20) to write the function (21) for the rhombic dodecahedron in the compact form

$$\phi(x, y, z) = \max(|x| + |y|, |x| + |z|, |y| + |z|).$$

For a fixed s, all the points in the space with $\phi(x, y, z) < s$ are the interior of the rhombic dodecahedron, $\phi(x, y, z) = s$ are on the rhombic dodecahedron and $\phi(x, y, z) > s$ are on the outside of the rhombic dodecahedron. Therefore for all $s \geq 0$ the function $\phi(x, y, z)$ describes concentric rhombic dodecahedra that are growing outside from the origin linearly with respect to s.

Using this fact, one can derive the function that is two at the center of the rhombic dodecahedron and decreases linearly to zero at the vertices, similar to the linear kernel described in Equation 14, to be:

$$L_{RD}(x, y, z) = 2 \max(0, 1 - \max(|x| + |y|, |x| + |z|, |y| + |z|)). \tag{22}$$

7 Results and Discussion

The optimality properties of the BCC sampling imply that the spectrum of a Cartesian sampled volume matches the spectrum of a BCC sampled volume with 29.3% fewer samples [7]. On the other hand, given equivalent sampling density per volume, the BCC sampled volume outperforms the Cartesian sampling in terms of information captured during the sampling operation. Therefore, in our test cases, we are comparing renditions of a Cartesian sampled dataset against renditions of an equivalently dense BCC sampled volume as well as against a BCC volume with 30% fewer samples.

In order to examine the reconstruction schemes discussed in this paper, we have implemented a ray-caster to render images from the Cartesian[5] and the BCC sampled volumetric datasets. The normal estimation, needed for shading, was based on central differencing of the reconstructed continuous function both in the Cartesian and BCC case. Central Differencing is easy to implement and there is no reason to believe that it performs any better or worse than taking the analytical derivative of the reconstruction kernel [10].

We have chosen the synthetic dataset first proposed in [9] as a benchmark for our comparisons. The function was sampled at the resolution of $40 \times 40 \times 40$ on the Cartesian lattice and at an equivalent sampling on the BCC lattice of $32 \times 32 \times 63$. For the sake of comparison with these volumes a 30% reduced volume of $28 \times 28 \times 55$ samples on the BCC lattice along with a volume of 30% increased sampling resolution of $44 \times 44 \times 44$ for the Cartesian sampling was also rendered. The images in Figure 7 are rendered using the cubic box spline on the BCC sampled datasets and the tri-cubic B-spline on the Cartesian sampled datasets. The images in Figure 8 document the corresponding error images that are obtained by the angular error incurred in estimating the normal (by central differencing) on the reconstructed function. The gray value of 255 (white) denotes the angular error of $30\,^\circ$ between the computed normal and the exact normal.

The optimality of the BCC sampling is apparent by comparing the images Figure 7(a) and Figure 7(b) as these are obtained from an equivalent sampling density over the volume. While the lobes are mainly preserved in the BCC case, they are smoothed out in the case of Cartesian sampling. This is also confirmed by their corresponding error images in Figure 8. The image in Figure 7(c) is obtained with a 30% reduction in the sampling density over the volume of the BCC sampled data while the image in Figure 7(d) is obtained with a 30% increase in the sampling density over the volume of the Cartesian sampled data. One could match the quality in Figure 7(c) with Figure 7(b) and the Figure 7(d) with the Figure 7(a), this pattern can also be observed in the error images of Figure 8. This matches our predictions from the theory of optimal sampling.

We also examined the quality of the linear kernel on this test function. The renditions of the test function using the linear kernel on the BCC lattice and tri-linear interpolation on the Cartesian lattice are illustrated in Figure 9. Since 98% of the energy of the test function is concentrated below the 41st wavenumber in the frequency domain [9], this sampling resolution is at a critical sampling rate and hence a lot of aliasing appears during linear reconstruction. We doubled the sampling rate on each dimension and repeated the

[5] In order to ensure fair comparison of Cartesian vs. BCC sampling we should compare our new reconstruction filters with filters based on the octahedron of first neighbors cell (see Section 4.1). However, tri-linear filtering is the common standard in volume rendering and since tri-linear filters are superior to the octahedron based filters, we will compare our new filters to the tensor-product spline family instead.

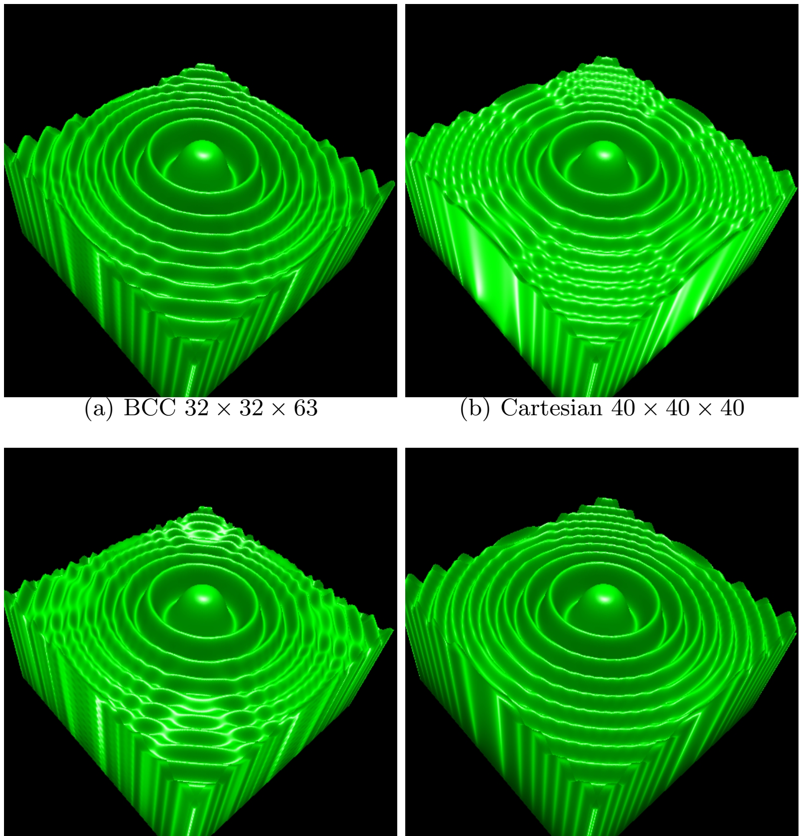

(a) BCC $32 \times 32 \times 63$

(b) Cartesian $40 \times 40 \times 40$

(c) BCC, 30% *reduced*

(d) Cartesian, 30% *increased*

Fig. 7. Comparison of BCC and Cartesian sampling of the Marschner-Lobb data set, cubic reconstruction

experiment in Figure 10. Figure 11 demonstrates the errors in the normal estimation. Due to the higher sampling density, the errors in normal estimation are considerably decreased; hence we have mapped the gray value 255 (white) to $5\,^{\circ}$ of error.

Renditions of the Marschner-Lobb function with this higher sampling resolution using cubic reconstruction and the corresponding error images are illustrated in Figure 12 and in Figure 13.

Throughout the images in Figure 7 through Figure 13, one can observe the superior fidelity of the BCC sampling compared to the Cartesian sampling.

Real volumetric datasets are scanned and reconstructed on the Cartesian lattice; there are filtering steps involved in scanning and reconstruction that tune the data according to the Cartesian sampling so the spectrum of the captured data is anti-aliased with respect to the geometry of the Cartesian

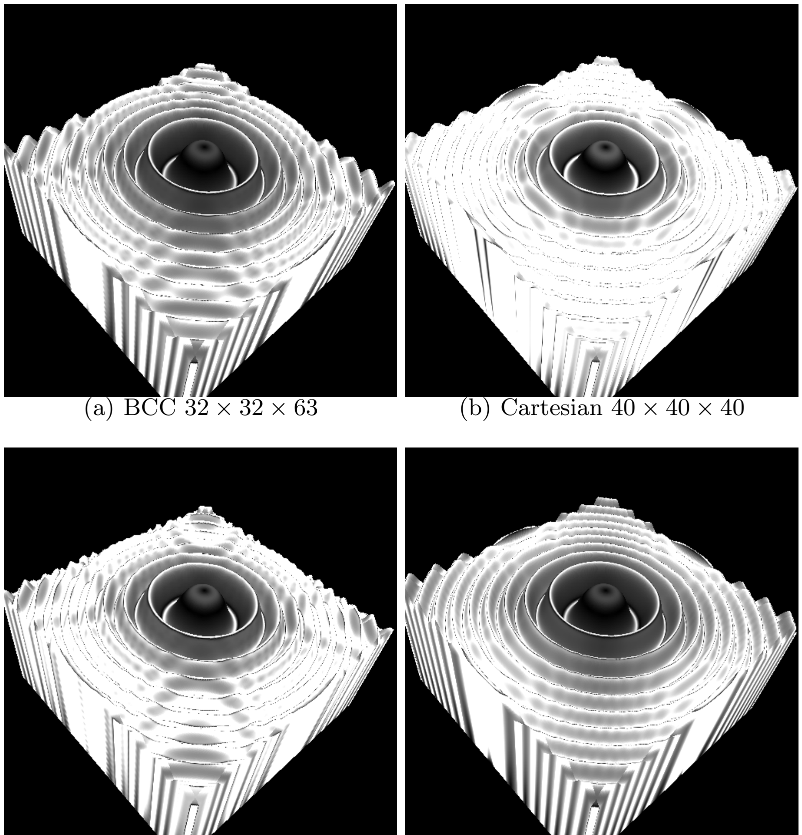

(a) BCC $32 \times 32 \times 63$ (b) Cartesian $40 \times 40 \times 40$

(c) BCC 30% *reduced* (d) Cartesian, 30% *increased*

Fig. 8. Angular error of the computed normal versus the exact normal of the cubic reconstruction in Figure 7. Angular error of 30° mapped to white

lattice. Therefore, the ultimate test of the BCC reconstruction can not be performed until there are optimal BCC sampling scanners available.

However, for examining the quality of our reconstruction filters on real world datasets we used a Cartesian filter to resample the Cartesian datasets on the BCC lattice. While prone to the errors of the reconstruction before resampling, we have produced BCC sampled volumes of the tooth and the UNC brain datasets with 30% reduction in the number of samples. The original tooth volume has a resolution of $160 \times 160 \times 160$ and the BCC volume after the 30% reduction has a resolution of $113 \times 113 \times 226$; similarly for the UNC dataset, the original Cartesian resolution of $256 \times 256 \times 145$ was reduced by 30% to the BCC resolution of $181 \times 181 \times 205$. The result of their rendering using the linear and the cubic box spline in the BCC case and the tri-linear and tri-cubic B-spline reconstruction in the Cartesian case is illustrated in

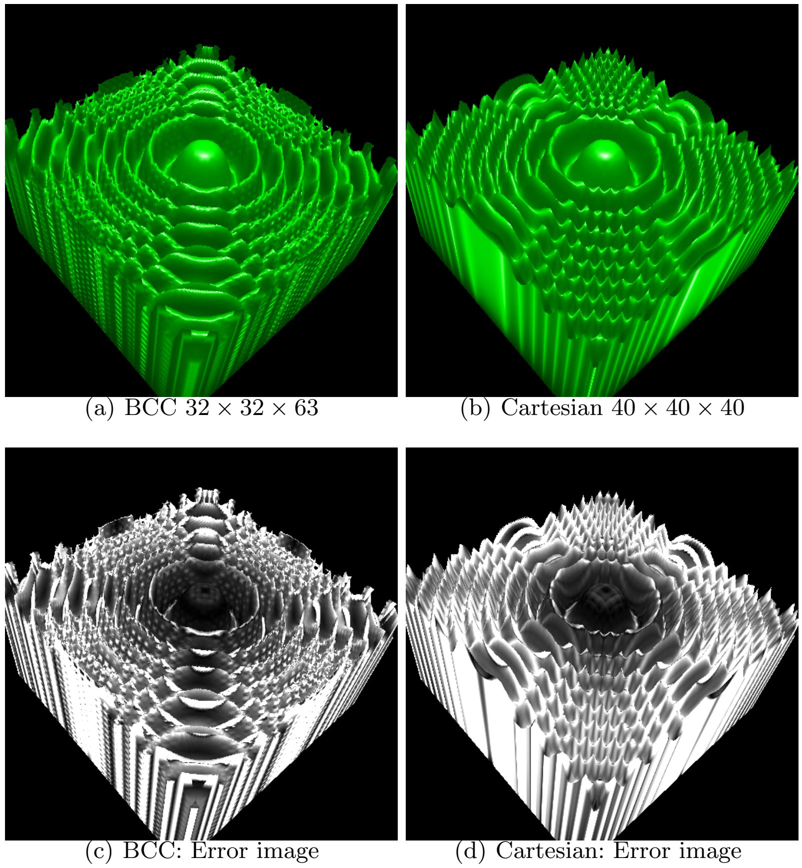

Fig. 9. (a,b)Comparison of BCC and Cartesian sampling of the Marschner-Lobb data set, linear reconstruction. (c,d) The corresponding error images map an angular error of 30° to white

Figure 14 and Figure 15. These images were rendered at a 512^2 resolution on an SGI Altix with sixty four 1.5GHz Intel Itanium processors running Linux.

8 Conclusion

In this paper we have derived an analytic description of linear and cubic box splines for the body centered cubic (BCC) lattice. Using geometric arguments, we have further derived a simplified analytical form of the linear box spline in Equation 22, which is simple and fast to evaluate (simpler than the trilinear interpolation function for Cartesian lattices).

Further we have also derived the analytical description of the Fourier transform of these novel filters and by demonstrating the number of vanishing mo-

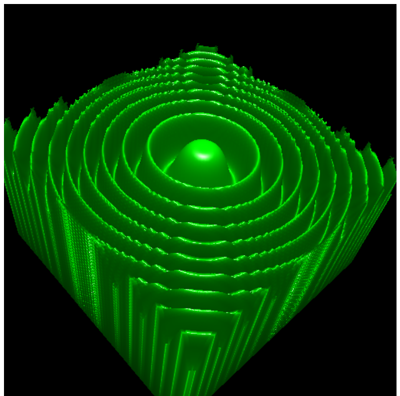

(a) BCC $64 \times 64 \times 126$

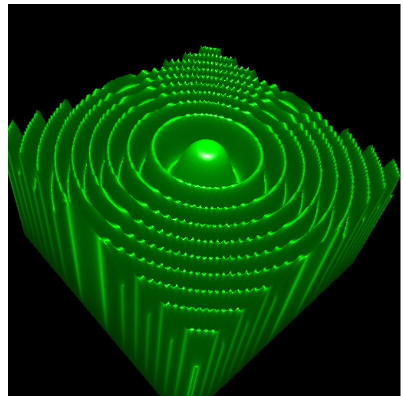

(b) Cartesian $80 \times 80 \times 80$

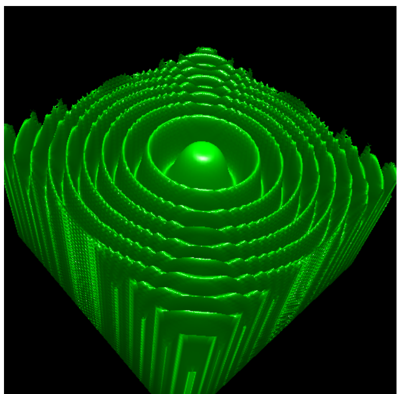

(c) BCC, 30% *reduced*

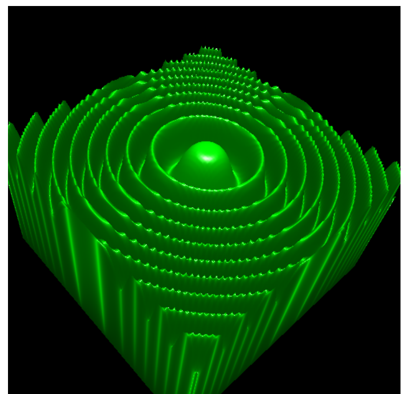

(d) Cartesian, 30% *increased*

Fig. 10. Linear reconstruction of the Marschner-Lobb data set at a higher resolution

ments we have established the numerical order of these filters. We believe that these filters will provide the key for a more widespread use of BCC sampled lattices.

Our images support the theoretical results of the equivalence of Cartesian lattices with BCC lattices of 30% fewer samples.

9 Future Research

As we have obtained the linear interpolation filter from projection of the tesseract, we can obtain odd order splines by successive convolutions of the linear kernel (or alternatively – projecting a tesseract which is the tensor product of higher order one-dimensional splines). However, the even order

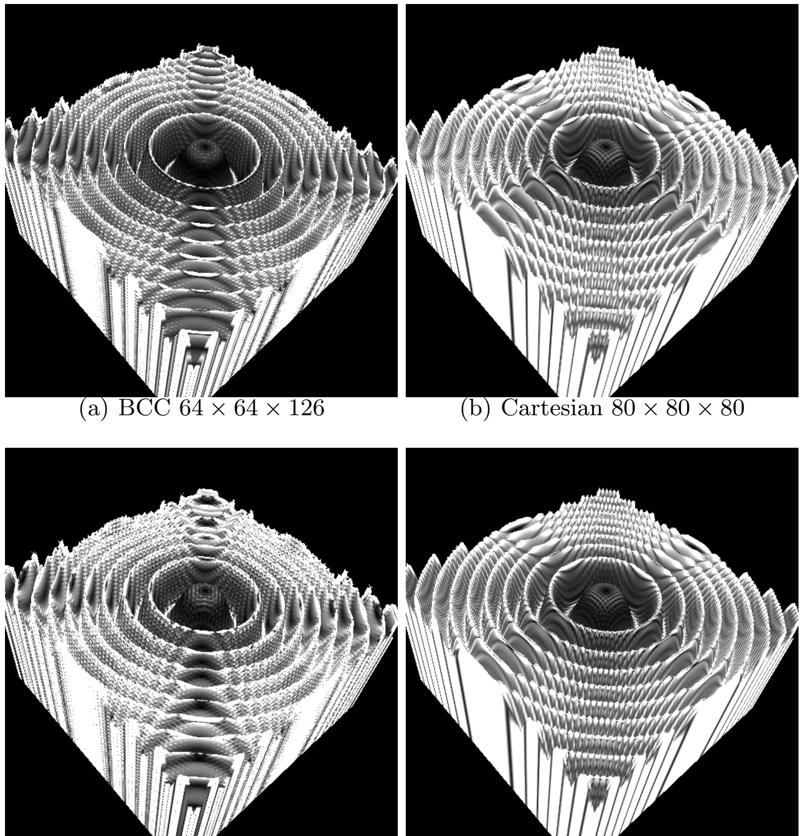

(a) BCC $64 \times 64 \times 126$ (b) Cartesian $80 \times 80 \times 80$

(c) BCC, 30% *reduced* (d) Cartesian, 30% *increased*

Fig. 11. Angular error images for linear reconstruction at a higher resolution as shown in Figure 10. Angular error of 5° mapped to white (255)

splines and their analytical forms do not seem to be easily derived. We are currently investigating this case.

The ease of deriving the frequency response of these interpolation filters lends itself to a thorough error analysis on this family.

Further, the computation of the cubic box spline in Equation 16 currently entails the evaluation of 81 terms. This makes the evaluation of the cubic kernel computationally expensive. We are currently investigating simplifications similar to that of the linear kernel discussed in Section 6.1.

Except for the first order box spline, the spline family are approximating filters, hence research on exact interpolatory filters, similar to those of Catmull-Rom for the BCC lattice is being explored.

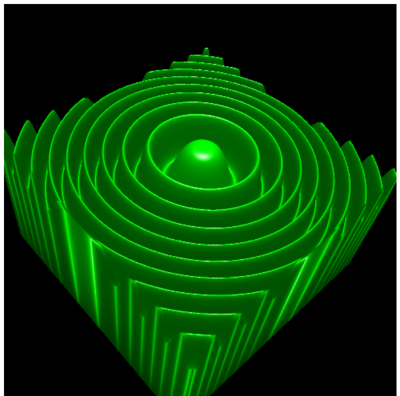

(a) BCC $64 \times 64 \times 126$

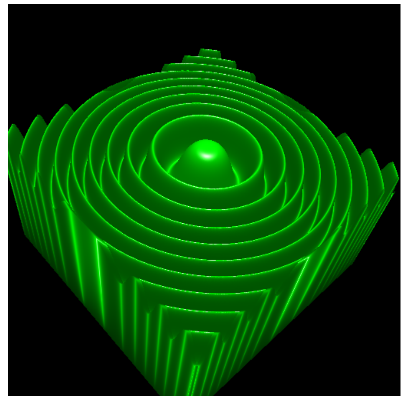

(b) Cartesian $80 \times 80 \times 80$

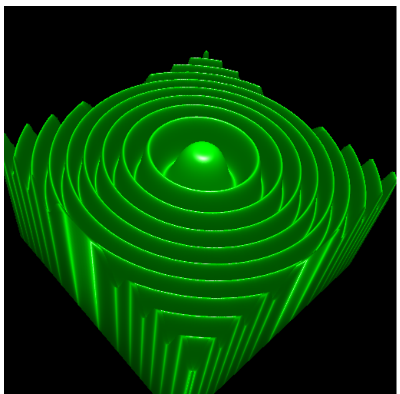

(c) BCC, 30% *reduced*

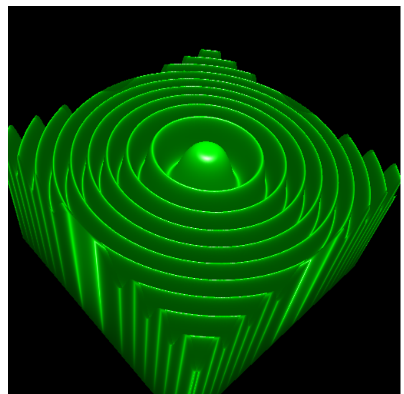

(d) Cartesian, 30% *increased*

Fig. 12. The cubic reconstruction of the Marschner-Lobb data set at a higher resolution

References

1. Pierre Brémaud. *Mathematical Principles of Signal Processing.* Springer, 2002.
2. Gerald Burns. *Solid State Physics.* Academic Press Inc., 1985.
3. J.H Conway and N.J.A. Sloane. *Sphere Packings, Lattices and Groups.* Springer, 3rd edition, 1999.
4. Carl deBoor, K Höllig, and S Riemenschneider. *Box splines.* Springer Verlag, 1993.
5. D. E. Dudgeon and R. M. Mersereau. *Multidimensional Digital Signal Processing.* Prentice-Hall, Inc., Englewood-Cliffs, NJ, 1st edition, 1984.
6. T.C. Hales. Cannonballs and honeycombs. *Notices of the AMS*, 47(4):440–449, April 2000.
7. Thomas Theußl, Torsten Möller, and Eduard Gröller. Optimal regular volume sampling. In *Proceedings of the IEEE Conference on Visualization 2001*, pages 91–98, Oct. 2001.

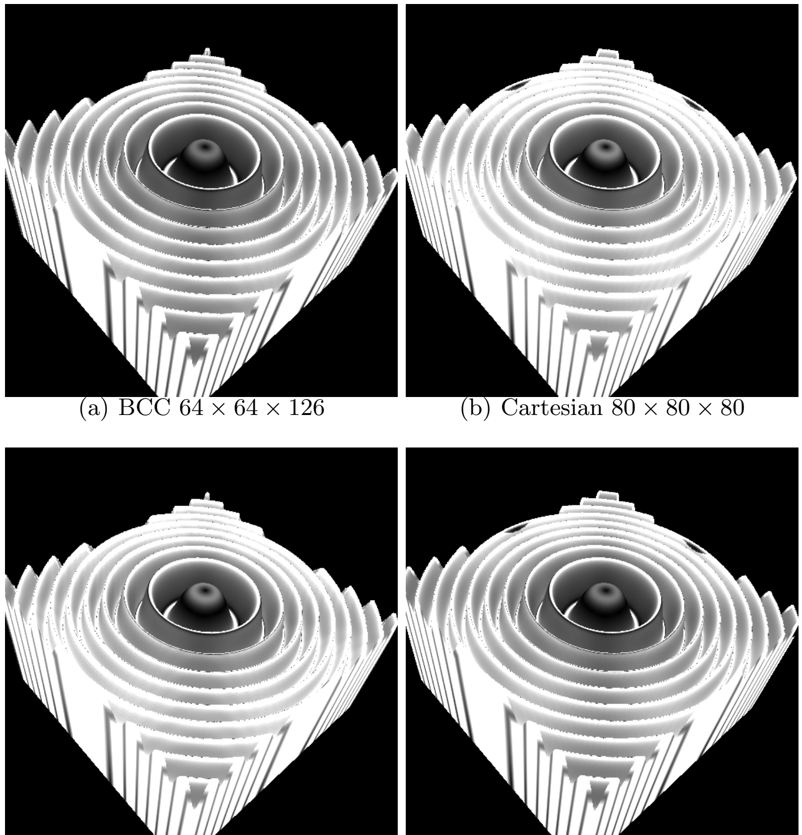

(a) BCC $64 \times 64 \times 126$ (b) Cartesian $80 \times 80 \times 80$

(c) BCC, 30% *reduced* (d) Cartesian, 30% *increased*

Fig. 13. Angular error images for cubic reconstruction at a higher resolution as shown in Figure 12. Angular error of 5° mapped to white (255)

8. Cornelius Lanczos. *Discourse on Fourier series*. New York, Hafner, 1966.
9. Steve R. Marschner and Richard J. Lobb. An evaluation of reconstruction filters for volume rendering. In R. Daniel Bergeron and Arie E. Kaufman, editors, *Proceedings of the IEEE Conference on Visualization 1994*, pages 100–107, Los Alamitos, CA, USA, October 1994. IEEE Computer Society Press.
10. Torsten Möller, Raghu Machiraju, Klaus Mueller, and Roni Yagel. A comparison of normal estimation schemes. In *Proceedings of the IEEE Conference on Visualization 1997*, pages 19–26, October 1997.
11. Gilbert Strang and George J. Fix. A Fourier analysis of the finite element variational method. *Construct. Aspects of Funct. Anal.*, pages 796–830, 1971.
12. Van De Ville, D., Blu, T., M. Unser, W. Philips, I. Lemahieu, and R. Van de Walle. Hex-splines: A novel spline family for hexagonal lattices. *IEEE Transactions on Image Processing*, 13(6):758–772, June 2004.

(a) BCC 30% reduced, linear box spline, 12 seconds

(b) Cartesian , tri-linear, 13 seconds

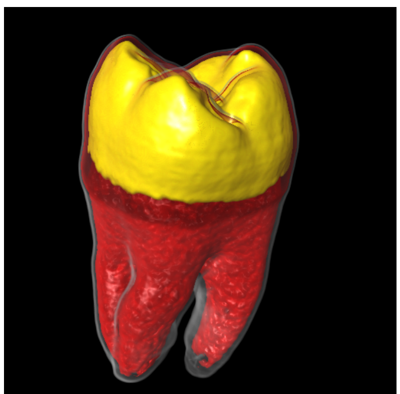

(c) BCC 30% reduced, cubic box spline, 190 minutes

(d) Cartesian, tri-cubic B-spline, 27 seconds

Fig. 14. The tooth dataset

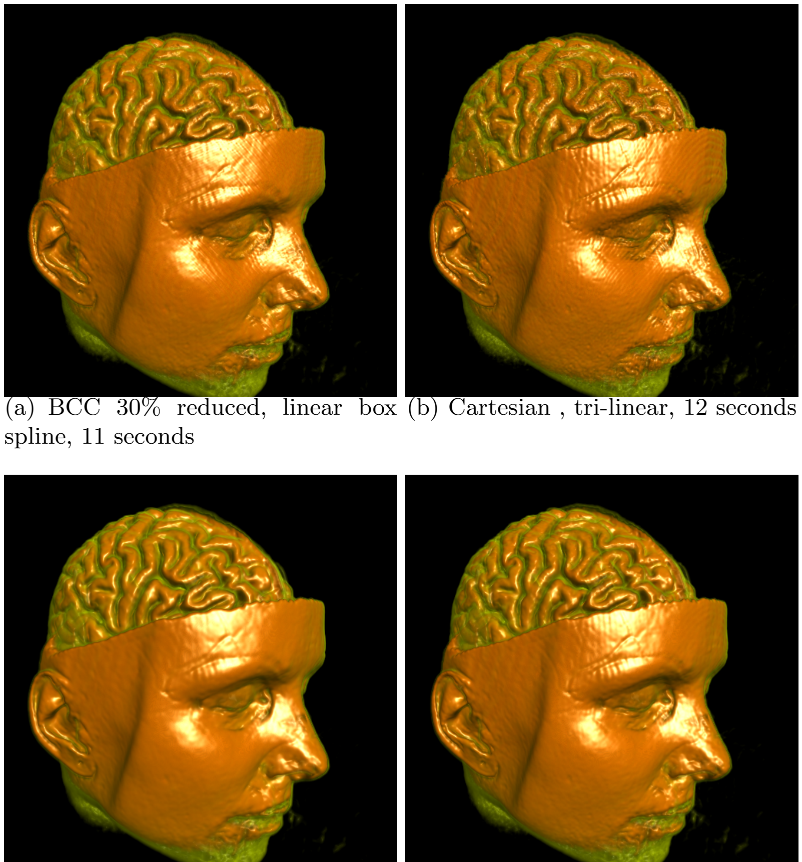

(a) BCC 30% reduced, linear box spline, 11 seconds

(b) Cartesian , tri-linear, 12 seconds

(c) BCC 30% reduced, cubic box spline, 170 minutes

(d) Cartesian, tri-cubic B-spline, 24 seconds

Fig. 15. The UNC dataset